Glassy Metal Alloy Nanofiber Anodes Employing Graphene Wrapping Layer: Toward Ultralong-Cycle-Life Lithium-Ion Batteries

Ji-Won Jung,[†] Won-Hee Ryu,[†,‡] Jungwoo Shin,[†,§] Kyusung Park,[⊥] and Il-Doo Kim*[,†]

[†]Department of Materials Science and Engineering, Korea Advanced Institute of Science and Technology, 291 Daehak-ro, Yuseong-gu, Daejeon 305-701, Republic of Korea, [‡]Department of Chemical and Environmental Engineering, Yale University, New Haven, Connecticut 06520-8286, United States, [§]Department of Materials Science and Engineering, University of Illinois at Urbana—Champaign, Urbana, Illinois 61801, United States, and [⊥]Texas Materials Institute, The University of Texas at Austin, Austin, Texas 78712, United States

ABSTRACT Amorphous silicon (a-Si) has been intensively explored as one of the most attractive candidates for high-capacity and long-cycle-life anode in Li-ion batteries (LIBs) primarily because of its reduced volume expansion characteristic (~280%) compared to crystalline Si anodes (~400%) after full Li^+ insertion. Here, we report one-dimensional (1-D) electrospun Si-based metallic glass alloy nanofibers (NFs) with an optimized composition of $Si_{60}Sn_{12}Ce_{18}Fe_5Al_3Ti_2$. On the basis of careful compositional tailoring of Si alloy NFs, we found that Ce plays the most important role as a glass former in the formation of the metallic glass alloy. Moreover, Si-based metallic glass alloy NFs were wrapped by reduced graphene oxide sheets (specifically $Si_{60}Sn_{12}Ce_{18}Fe_5Al_3Ti_2$ NFs@rGO), which can prevent the direct exposure of a-Si alloy NFs to the liquid electrolyte and stabilize the solid-electrolyte interphase (SEI) layers on the surfaces of rGO sheets while facilitating electron transport. The metallic glass nanofibers exhibited superior electrochemical cell performance as an anode: (i) $Si_{60}Sn_{12}Ce_{18}Fe_5Al_3Ti_2$ NFs show a high specific capacity of 1017 mAh g^{-1} up to 400 cycles at 0.05C with negligible capacity loss as well as superior cycling performance (nearly 99.9% capacity retention even after 2000 cycles at 0.5C); (ii) $Si_{60}Sn_{12}Ce_{18}Fe_5Al_3Ti_2$ NFs@rGO reveals outstanding rate behavior (569.77 mAh g^{-1} after 2000 cycles at 0.5C and a reversible capacity of around 370 mAh g^{-1} at 4C). We demonstrate the potential suitability of multicomponent a-Si alloy NFs as a long-cycling anode material.

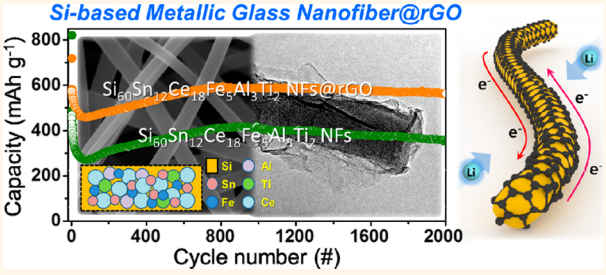

KEYWORDS: lithium-ion battery · amorphous silicon · metallic glass · alloy · electrospinning · nanofiber

Silicon (Si) is a promising anode material for lithium-ion batteries because of its high theoretical capacity (4200 mAh g^{-1} for $Li_{4.4}Si$ phase), which is approximately 11 times higher than that (372 mAh g^{-1}) of a commercial graphite anode.[1] However, crystalline Si (c-Si) undergoes fracturing and pulverization due to severe volume changes (~400%)[2,3] during cycling, which originate from the large uptake of Li ions (maximum 4.4 per Si atom).[4] In addition, the severe volume expansion/contraction of Si ruptures the solid-electrolyte interphase (SEI) layer formed on the surface of the Si electrode during cycling.[5,6] As a result, the fresh Si surface created by pulverization can be repeatedly exposed to the electrolyte during cycling, resulting in the additional formation of an irregular SEI layer. This causes a significant increase in the cell resistance due to the nonuniform and continuous growth of the SEI layer, leading to the deterioration of the cell capacity and degradation of the cycle performance.[7,8]

It is well-known that Li^+ insertion/extraction into crystalline Si induces considerable mechanical strain according to a two-phase reaction in which c-Si is consumed to form an amorphous Li_xSi (a-Li_xSi) alloy through an electrochemical solid-state amorphization process.[9,10] Intriguingly, the first lithiation reaction mechanism of amorphous Si (a-Si) is similar to the two-phase reaction which takes place during the lithiation of c-Si, but its fracturing and pulverization are largely suppressed and the lithiation reaction time

* Address correspondence to idkim@kaist.ac.kr.

Received for review March 5, 2015 and accepted May 31, 2015.

Published online May 31, 2015
10.1021/acsnano.5b01402

(or speed) is shorter (faster) than that in c-Si.[11] These characteristics mean that the critical particle size of a-Si based anode materials before fracturing is much larger than that of c-Si and that the lithiation rate is not as sluggish as it is in the case of c-Si. This is mainly due to its isotropic reaction characteristics of a-Si, with a lower Li concentration in the alloy phase during lithiation and lower energy barriers (<0.50 eV) for Li diffusion pathways.[12] Moreover, after the first cycle, a-Si undergoes a subsequent lithiation process *via* a single-phase reaction, allowing homogeneous lithiation without the formation of a heterogeneous interphase. In this sense, the use of a-Si based anode materials is highly desirable for enabling the commercial implementation of lithium-ion batteries with longer cycle lifetimes.

The amorphous, metallic glass nature is a disordered phase composed of a large free-volume zone. Here, the free-volume zone refers to a loosely bonded atomistic vacancy that is elastically enveloped by metallic alloy atoms.[13,14] The metallic glass has a high elastic strain limit, which makes it possible to enhance the mechanical properties and to increase the lithium storage limit. Therefore, various approaches have thus far been suggested for the synthesis of amorphous Si-based anode materials.[15,16] For example, Si-based metallic glass alloys were prepared by strategic additions of various elements.[17] Dahn's and Obrovac's groups reported a variety of examples based on (1) binary components of Si-M such as $Si_{0.66}Sn_{0.34}$, or (2) ternary components of Si-M_1-M_2 containing 20−40 at. % of M_1 and 15−20 at. % of M_2 (M_1 = Sn, Al, transition metals; M_2 = lanthanum or cerium).[18−24] The optimized composition of Si and other metallic elements could induce the amorphous, metallic glass phase that is beneficial to deliver high capacity levels and stable cycle performance. For ternary alloys such as SiAlSn, the Si component plays a main role in storing lithium. Moreover, Sn contributes to facile electronic/ionic transfers and partially to the capacity, while Al serves as a functional phase stabilizer to form an amorphous Si alloy. In addition, the selective substitution of inactive elements such as Fe and Ti has been suggested with regard to a trade-off relationship between the capacity and the cyclability (here, the energy density of an a-Si based active/inactive anode using the entire voltage range is not considered).[25] When excessive Sn is added to the Si alloys, capacity fading gradually occurs during cycling primarily because Sn remains as a crystallized species, preferentially becoming segregated in the amorphous matrix.[26] Therefore, the segregated Sn species induce volume expansion during cycling.[27] To overcome this problem, rare-earth metals such as cerium (Ce), lanthanum (La) and praseodymium (Pr) have been considered as functional additives for the effective suppression of the local segregation of crystalline Sn in Si alloys.[22] Importantly, Si alloys containing rare-earth metals exhibit low glass-forming temperatures, facilitating the stabilization of the metallic glass phase. As an ultimate Si-based metallic glass material for high capacity and a long-cycling anode, in early 2007 the 3 M company suggested a multicomponent metallic alloy with the composition of $Si_{60}Al_{14}Fe_8Ti_1Sn_7(MM)_{10}$ (MM = misch metal).[28]

Besides compositional considerations, morphological control of the metallic glass material, particularly Si-based metallic alloys in a low-dimensional structure, is also essential to obtain a higher elastic strain limit and improve the electrochemical performance.[29−32] Thus, far a number of researchers have investigated nanostructures with high surface areas and high porosity levels which can facilitate electrochemical reactions and the amount of electrolyte uptake.[33−36] Most Si-based nanostructures, consisting of various metallic components, are synthesized *via* high-temperature chemical vapor deposition (CVD) or sputtering.[16,37−39] However, challenging issues regarding the complexity of the synthetic process and difficulty in scalability remain. Meanwhile, the electrospinning technique has been considered as a facile and economical method with which to fabricate one-dimensional (1-D) nanofibers (NFs) for energy storage applications.[40−42] 1-D NFs can provide a large surface area and numerous pore channels between the fibers for excellent electrolyte permeability and good stress/strain accommodation during cycling.[43] Moreover, the introduction of graphene layers into NFs can further stabilize the electrochemical interface and hence improve the Coulombic efficiencies and cycle life, as our previous research demonstrated graphene wrapping on conducting carbon nanofiber-embedded Si nanoparticles.[44] The Si-based metallic glass alloy-core/graphene-shell can suppress the direct growth of the SEI layer on the Si surface, showing a tendency to form a thin and stable SEI layer on top of a graphene overcoating layer.

In this work, we report Si-based multicomponent amorphous alloy $Si_{60}Sn_{12}Ce_{18}Fe_5Al_3Ti_2$ nanofibers employing graphene wrapping layer (hereafter, $Si_{60}Sn_{12}Ce_{18}Fe_5Al_3Ti_2$ NFs@rGO). The Si-based metallic glass alloy NFs encapsulated by graphene sheets offer several key advantages over pristine a-Si: (i) a low-strain structure resulting from its unique 1-D amorphous alloy nature, (ii) a thin and stable SEI layer without abnormal growth and/or breakage, and (iii) enhanced electrical performance due to its highly conductive graphene network. To the best of our knowledge, this is the first demonstration of 1-D Si-based metallic glass alloy NFs as an anode material which includes an amorphous Sn (a-Sn) additive *via* an electrospinning route. Here, we synthesized three-component (Si, Sn and Al), four-component (Si, Sn, Al and Fe) five-component (Si, Sn, Al, Fe and Ce), and six-component Si alloy NFs to determine the microstructural evolution characteristics as a function of the composition. The potential suitability of electrochemically stable

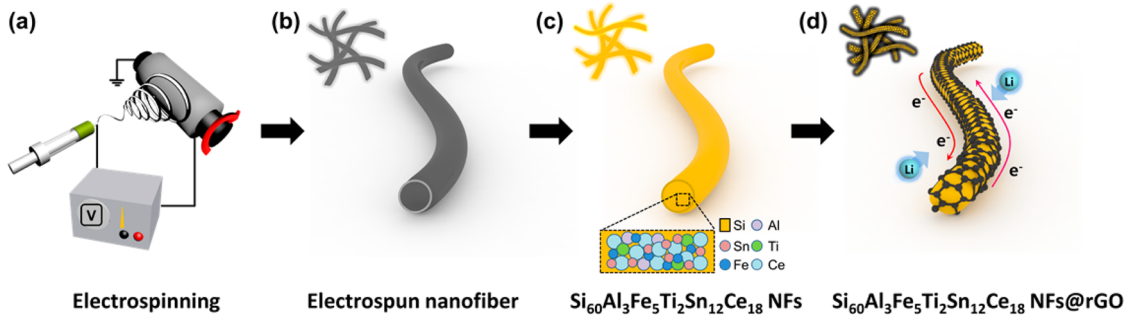

Scheme 1. Schematic illustrations of the synthesis of the graphene-wrapped $Si_{60}Al_3Fe_5Ti_2Sn_{12}Ce_{18}$ NFs ($Si_{60}Sn_{12}Ce_{18}Fe_5Al_3Ti_2$ NFs@rGO): (a) electrospinning process; (b) as-spun NFs; (c) thermal annealing; (d) hybrid self-assembly between the $Si_{60}Sn_{12}Ce_{18}Fe_5Al_3Ti_2$ NFs and the GO, and the subsequent chemical reduction.

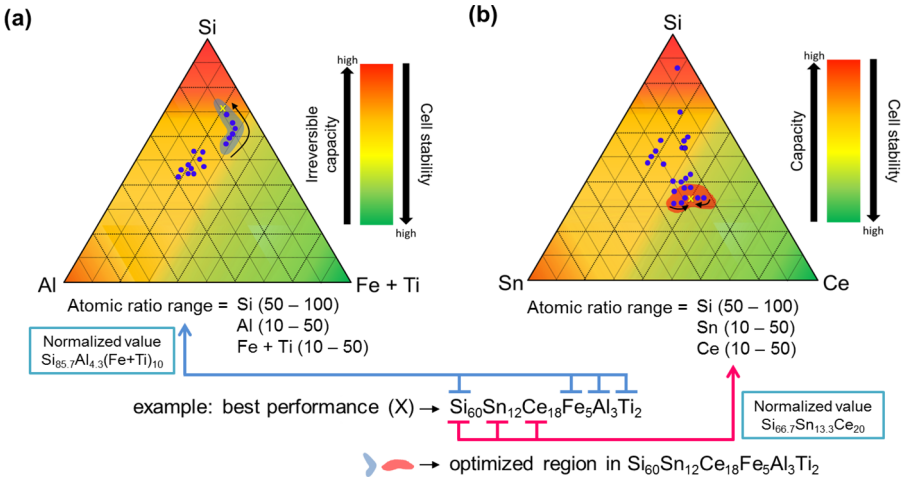

Figure 1. Optimization of the Si-based metallic glass alloy NF in light of the lithium storage performance. The schematic compositional diagrams exhibit general correlation between compositions and electrochemical performances: (a) (Si, Al and [Fe+Ti]) and (b) (Si, Sn, and Ce). All data are based on the relative atomic ratio of the specific elements involved. Note that it just shows a general behavior within our experimental data, and the color code does not necessarily reflect real performances.

$Si_{60}Sn_{12}Ce_{18}Fe_5Al_3Ti_2$ NFs as a long-cycle-life anode material is discussed.

RESULTS AND DISCUSSION

Synthesis of the $Si_{60}Sn_{12}Ce_{18}Fe_5Al_3Ti_2$ NFs Employing Graphene Wrapping Layer. The synthetic procedures used to create the graphene-wrapped Si-based metallic glass alloy NFs are schematically illustrated in Scheme 1. Initially, 1-D electrospun $Si_{60}Sn_{12}Ce_{18}Fe_5Al_3Ti_2$ precursor/polyvinylpyrrolidone (PVP) composite fibers were prepared *via* electrospinning (Scheme 1a,b) and annealing at 700 °C in an H_2/N_2 atmosphere (Scheme 1c), resulting in the formation of amorphous $Si_{60}Sn_{12}Ce_{18}Fe_5Al_3Ti_2$ NFs. Then, 3-aminopropyltriethoxysilane (APS) was grafted onto the surfaces of the heat-treated fibers, resulting in $Si_{60}Sn_{12}Ce_{18}Fe_5Al_3Ti_2$ NFs with a positively charged surface state. Subsequently, the $Si_{60}Sn_{12}Ce_{18}Fe_5Al_3Ti_2$ NFs were wrapped by negatively charged graphene oxide (GO) in an aqueous solution by electrostatic interaction. Finally, rGO-wrapped $Si_{60}Sn_{12}Ce_{18}Fe_5Al_3Ti_2$ NFs ($Si_{60}Sn_{12}Ce_{18}Fe_5Al_3Ti_2$ NFs@rGO) were synthesized by a chemical reduction process using hydrazine (Scheme 1d). The weight of the residual elements was dramatically decreased after a high temperature calcination and proper washing, and the abbreviation here for $Si_{60}Sn_{12}Ce_{18}Fe_5Al_3Ti_2$ NFs is based on the major metallic elements, excluding the effect of residual elements which do not affect continuous electrochemical performance at all (Table S1, Supporting Information).

Compositional Optimization of $Si_{60}Sn_{12}Ce_{18}Fe_5Al_3Ti_2$ Nanofibers. In order to optimize the electrochemical advantages of the six-component a-Si NFs, started from a previously reported composition,[28] we tuned and carefully tailored the composition of the Si-based metallic glass NFs, as presented in Figure 1 and Table S2. Among plenty of compositions presented in Table S2, several representative compositions are expressed by the blue dots, so as to avoid a confusion. The triangles organize a relationship between compositional ratio of elements and their electrochemical performances (capacity *versus* cyclability) and is based on electrochemical behavioral tendency of such compositions. The triangle phase diagrams can be interpreted as the

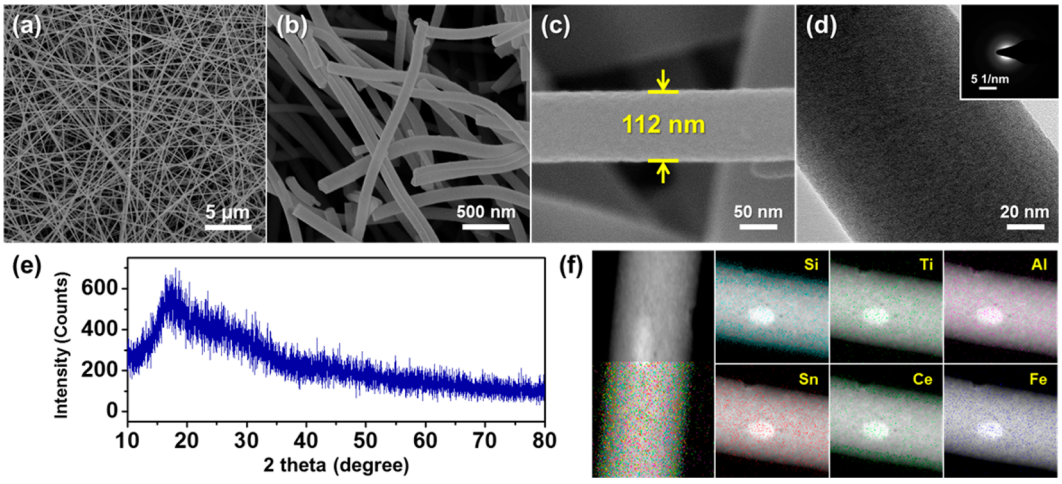

Figure 2. (a) SEM image of the as-spun $Si_{60}Sn_{12}Ce_{18}Fe_5Al_3Ti_2$ NFs. (b,c) SEM images, (d) TEM image (the inset in (d) shows the corresponding SAED pattern) and (e) X-ray diffraction pattern of the thermally annealed $Si_{60}Sn_{12}Ce_{18}Fe_5Al_3Ti_2$ NFs. (f) Scanning transmission electron microscopy (STEM) and EDS-mapping of the individual elements in the $Si_{60}Sn_{12}Ce_{18}Fe_5Al_3Ti_2$ NFs.

following way: the atomic ratio of Si, Sn and Ce in the $Si_{60}Sn_{12}Ce_{18}Fe_5Al_3Ti_2$ NFs which showed the best performance can be converted into a normalized value, *i.e.*, $Si_{66.7}Sn_{13.3}Ce_{20}$ for specific three components, which is point "X" in the optimized region (Figure 1). First, the atomic ratio of Al decreased precisely from Al_{14} to Al_3 considering the poor capacity retention of pure Al. Although Al can have an the effect of suppressing the crystalline phase in an amorphous matrix, which is the prime requirement for the cyclability of electrochemical cells, its significant irreversible loss of capacity indeed limits the elemental concentration of Al. On the other hand, an increase in the amount of Si as a major active element leads to rapid capacity fading, which can be attributed to a loss of electrical contact resulting from the considerable volume expansion. This explains the fixed atomic ratio of Si. The inactive buffer phase should be compatible with electroactive Si and have a high tensile strength so that it may effectively absorb the massive volume changes of the active material during the lithiation process.[25] To meet these requirements, Ti and Fe were chosen as inactive elastic matrix formers,[18] but their atomic ratio was tuned in consideration of the trade-off between the active and inactive phases. Interestingly, the most critical aspect of the compositional optimization is balancing the atomic ratio of Sn and Ce. When the atomic percent of Sn is extremely high compared to that of Ce, *i.e.*, $Si_{60}Sn_{14}Ce_7Fe_8Al_{10}Ti_1$, the Sn is exclusively extracted from the amorphous matrix, which is detrimental to stable capacity retention due to the large volume changes induced by Sn nanocrystallites (nc-Sn) (Figure S1). In contrast, Si-based metallic glass NFs with a sufficient amount of Ce to promote amorphization could prevent Sn aggregation.[23] Finally, we pinpointed well-balanced Si alloy NFs, with a composition of $Si_{60}Sn_{12}Ce_{18}Fe_5Al_3Ti_2$.

Microstructural and Phase Characterization of $Si_{60}Sn_{12}Ce_{18}Fe_5Al_3Ti_2$ Nanofibers. The morphologies of the $Si_{60}Sn_{12}Ce_{18}Fe_5Al_3Ti_2$ NFs are shown in Figure 2. The as-spun fibers exhibited an average diameter of *ca*. 200 nm with a uniform distribution of the fibers (Figure 2a). After calcination at 700 °C in an atmosphere of 5% H_2 and 95% N_2, continuous and interconnected $Si_{60}Sn_{12}Ce_{18}Fe_5Al_3Ti_2$ NFs with an average diameter of 100 nm were obtained (Figure 2b–d). The reduction in the diameter of the final $Si_{60}Sn_{12}Ce_{18}Fe_5Al_3Ti_2$ NFs is mainly attributable to the decomposition of metal-salt precursors and the PVP matrix polymer during the high-temperature calcination step. The annealed $Si_{60}Sn_{12}Ce_{18}Fe_5Al_3Ti_2$ NFs exhibited a smooth surface without the aggregation of any reduced metal particles. Metallic Sn has a relatively low melting temperature of 231.9 °C; therefore, it is easily segregated into agglomerates at a high temperature.[26,45,46] We speculate that the main reason behind this abnormal behavior with a homogeneous distribution of Sn atoms is a synergistic effect through a combination of a unique composition and an electrospinning process, which will be discussed in detail later. Figure 2d shows a transmission electron microscopy (TEM) image and the corresponding selected-area electron diffraction (SAED) pattern (inset) of the $Si_{60}Sn_{12}Ce_{18}Fe_5Al_3Ti_2$ NFs, indicating that no crystalline lattice fringes of $Si_{60}Sn_{12}Ce_{18}Fe_5Al_3Ti_2$ NFs were observed. The X-ray diffraction data in Figure 2e as well as the SAED pattern also shows no evidence of crystallization, which confirms the amorphous nature of the $Si_{60}Sn_{12}Ce_{18}Fe_5Al_3Ti_2$ NFs. Moreover, energy-dispersive X-ray spectroscopy (EDS) elemental maps of the $Si_{60}Sn_{12}Ce_{18}Fe_5Al_3Ti_2$ NFs clearly verified a homogeneous distribution of each element (Figure 2f).

Electrochemical Characterization of $Si_{60}Sn_{12}Ce_{18}Fe_5Al_3Ti_2$ Nanofibers. In order to investigate the intrinsic electrochemical

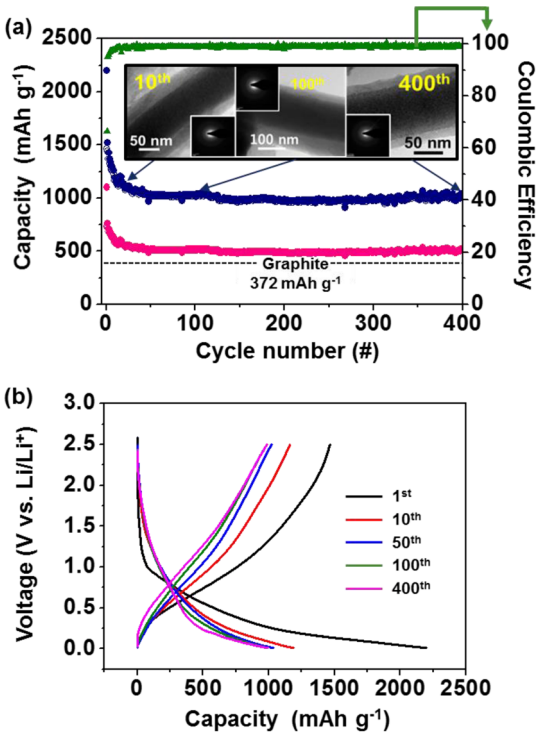

Figure 3. (a) Charge/discharge cycle performances of the $Si_{60}Sn_{12}Ce_{18}Fe_5Al_3Ti_2$ NFs at a 0.05C rate (50 mA g^{-1}) for 400 cycles. Insets correspond to *ex situ* TEM images after cycling 10, 100, and 400 times. The capacities were calculated on the basis of (pink circles) the total weight of the electrode and (navy circles) the weights of active elements (Si and Sn); and (b) the corresponding voltage profiles of the $Si_{60}Sn_{12}Ce_{18}Fe_5Al_3Ti_2$ NFs at different cycles.

performance capabilities of pristine $Si_{60}Sn_{12}Ce_{18}Fe_5Al_3Ti_2$ NFs as an anode material with a long cycle and high performance levels, coin-type half-cells with Li counter electrodes were tested. We do not dispute that other variables such as binder and electrolyte additives are of great importance in considering the detachment of active materials from current collector and the preformed stable SEI layer, so as to precisely explore an original electrochemical properties of the $Si_{60}Sn_{12}Ce_{18}Fe_5Al_3Ti_2$ NFs. As shown in Figure 3a, the first and second discharge capacities of the $Si_{60}Sn_{12}Ce_{18}Fe_5Al_3Ti_2$ NFs were 2201 and 1464 mAh g^{-1}, respectively, in a voltage range of 0.01−2.5 V at 0.05C (corresponding to 50 mA g^{-1}). The irreversible capacity loss (737 mAh g^{-1}) after the first cycle was mainly attributed to the formation of the irreversible SEI layers, the loss of local structural integrity by the volume change, and to the irreversible lithium loss caused by thin surface SiO_x species (Figure S2 and Figure S3) with a small oxygen component (5 wt % in the NFs) as measured in an elemental analysis.[47] A stabilized Coulombic efficiency (CE) ratio of 98.23% was obtained after the first ten cycles. Although a continuous capacity drop was observed up to 50 cycles, its reversible capacity (1017 mAh g^{-1}, 99%, excellent capacity retention from 50 to 400 cycles) was nearly 2.7 times higher than that of conventional graphite (a detailed discussion is given in Figure S4). More importantly, the $Si_{60}Sn_{12}Ce_{18}Fe_5Al_3Ti_2$ NFs exhibited excellent cycling performance for nearly one year, completing 400 cycles at 0.05C without a further capacity loss. For a closer investigation of the electrochemical stability at the interface between the NFs and the liquid electrolyte, we carried out an *ex situ* TEM analysis on each of the cells after 10, 100, and 400 cycles (insets in Figure 3a). The measured thickness of the SEI layer was approximately 30 nm upon the 10th cycle, and this level was maintained up to 400th cycle without a further increase in the thickness. No active-metal-particle agglomeration or exclusion out of the fibers was observed, indicating an electrochemically stable surface as well as a retained metallic glass phase during the charge/discharge process. These results suggest the potential for excellent Coulombic efficiency levels and long cycle lifetimes. Figure 3b shows the charge/discharge voltage curves of $Si_{60}Sn_{12}Ce_{18}Fe_5Al_3Ti_2$ NFs at different cycles. Upon the initial discharge, electrolyte decomposition and the subsequent formation of a SEI layer took place, corresponding to a sloping curve between 1.0 and 0.5 V. Subsequently, continuous and smooth charge/discharge voltage curves were observed without any voltage plateau, which reflects the amorphous nature of the active material.[48] Moreover, even after 400 cycles, there were no notable changes in the voltage curves. As shown in Figure 2f, a homogeneous and uniform atomic distribution of the active/inactive elements should not only mechanically support the active materials but also prevent the active materials from aggregation during cycling. The stable SEI layer played an important role in the superior cycling performance. These observations imply that the compositional optimization of Si-based alloy electrodes is of great importance for ensuring a very long cycle lifetime.

Important Role of Ce for Metallic Glass Alloy Nanofibers without Sn Segregation. The $Si_{60}Sn_{12}Ce_{18}Fe_5Al_3Ti_2$ NFs showed superior performance characteristics considering the critical electrochemical parameters such as the reversible and irreversible capacities, the Coulombic efficiencies, and the cyclability. For a clearer understanding of the mechanism underlying the synthesis of fully amorphous Si alloy NFs without Sn segregation, we examined several compositions, *i.e.*, $Si_{80}Sn_{16}Al_4$, $Si_{75}Sn_{15}Al_{3.75}Fe_{6.25}$, and $Si_{61.22}Sn_{12.25}Al_{3.06}Fe_{5.1}Ce_{18.37}$ (Figure S5). The chemical formula of the Si-alloy NFs was normalized to each element, as derived from $Si_{60}Sn_{12}Ce_{18}Fe_5Al_3Ti_2$ NFs through the exclusion of specific elements (see details in the Supporting Information), and a quantitative investigation of multicomponent NFs was confirmed by an inductively coupled plasma (ICP) composition analysis (Table S3). In general, Sn is thermodynamically not compatible with several systems, including our system with a low amount of Ce-driven Si-based metallic glass NFs,

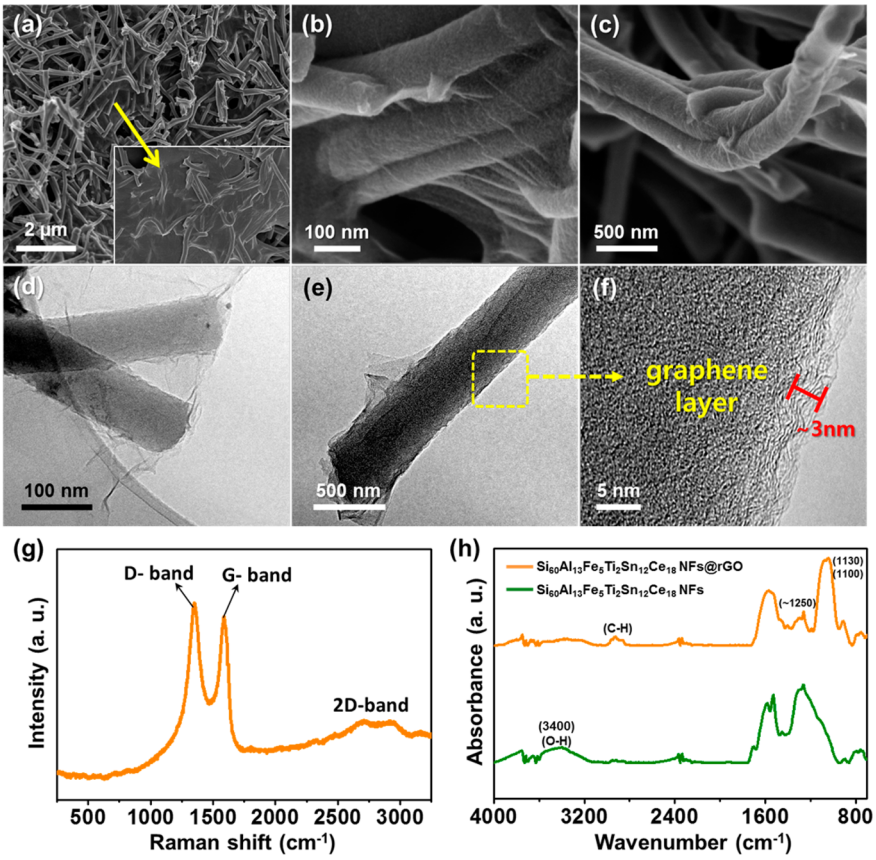

Figure 4. (a) Low-magnification SEM image and (b,c) high-magnification SEM images showing a few strands of NFs that tended to be coated with broad graphene sheets (yellow allow and individual NFs well covered by the flexible graphene, respectively. (d) TEM image of $Si_{60}Sn_{12}Ce_{18}Fe_5Al_3Ti_2$ NFs@rGO corresponding to (b), and (e,f) TEM image of $Si_{60}Sn_{12}Ce_{18}Fe_5Al_3Ti_2$ NFs@rGO corresponding to (c). (g) Raman spectrum of the $Si_{60}Sn_{12}Ce_{18}Fe_5Al_3Ti_2$ NFs@rGO and (h) FT-IR spectra of the $Si_{60}Sn_{12}Ce_{18}Fe_5Al_3Ti_2$ NFs and the $Si_{60}Sn_{12}Ce_{18}Fe_5Al_3Ti_2$ NFs@rGO.

as mentioned above. In order to avoid the agglomeration of Sn before and after the reaction with Li^+, numerous methods have been suggested to confine the Sn atoms in highly qualified matrix using electrospinning or alloy quenching processes, but none could prevent Sn crystallization inside and/or outside of the matrices.[49,50] Interestingly, Sn and a sufficient Ce addition to a Si-based alloy along with a rapid solidification technique such as the melt-spinning process can could stop the expulsion of crystalline Sn from a Si-based metallic glass alloy.[23,24] As shown in Figure S5, the Sn nanoparticles were precipitated on the surfaces of the NFs in both $Si_{80}Sn_{16}Al_4$ and $Si_{75}Sn_{15}Al_{3.75}Fe_{6.25}$ NFs calcined at 700 °C. The XRD patterns in Figure S5j are in good agreement with the standard positions of the Sn phase (JCPDS 65−2631). In contrast, $Si_{61.22}Sn_{12.25}Al_{3.06}Fe_{5.1}Ce_{18.37}$ NFs including sufficient Ce showed very smooth surface morphologies without the formation of Sn particles (Figure S5h,i). We speculate that the mechanism of the homogeneous Sn distribution can be interpreted as a result of the limited Sn diffusion during calcination by the presence of less mobile Ce as a neighbor. This is main reason for electrochemically stable electrodes with Ce (see details in Figure S6).

Morphological Evolution of Reduced Graphene Oxide (rGO) Wrapping Layer on the Surface of $Si_{60}Sn_{12}Ce_{18}Fe_5Al_3Ti_2$ Nanofibers and Materials Characterization. Although the $Si_{60}Sn_{12}Ce_{18}Fe_5Al_3Ti_2$ NFs exhibited good capacity retention for more than 400 cycles (Figure 3a), the relatively thickness of the observed SEI layer (about 40 nm) compared to the diameter of the NFs must be reduced to reduce the cell resistance and improve the electrochemical kinetics. In order to suppress the degree of electrolyte decomposition and effectively control the SEI formation on the surfaces of the NFs, we introduced a flexible, smooth and conductive graphene sheet as a wrapping layer for $Si_{60}Sn_{12}Ce_{18}Fe_5Al_3Ti_2$ NFs, thereby remarkably suppressing the formation of insulating SEI layers. Figure 4a−c exhibit SEM images of $Si_{60}Sn_{12}Ce_{18}Fe_5Al_3Ti_2$ NFs@rGO. Aggregation of the graphene sheets was not observed owing to the use of electrostatic attraction between the APS-treated positively charged NFs and the negatively charged graphene sheets.[44] The NFs are partially interconnected by large graphene sheets (see the yellow arrow in Figure 4a). As shown in the TEM image in Figure 4d, several bundles of NFs were covered by graphene sheets. Individual NFs were wrapped by stacked graphene sheets with a thickness of approximately 3 nm (Figure 4e,f).

To find chemical evidence of graphene wrapping, we carried out Raman spectroscopy and Fourier transform infrared spectroscopy (FT-IR) analysis (Figure 4g,h). Figure 4g shows the Raman spectrum of the $Si_{60}Sn_{12}Ce_{18}Fe_5Al_3Ti_2$ NFs@rGO to verify the graphene sheet. The peaks at about 1350 and 1590 cm^{-1} are assigned to the D and G band peaks of the graphene sheets, which clearly represent the presence of a carbon layer. In the FT-IR spectra presented in Figure 4h, the pristine $Si_{60}Sn_{12}Ce_{18}Fe_5Al_3Ti_2$ NFs shows a peak at 3400 cm^{-1} for the O—H stretching vibration of silicon oxide, which disappears after APS modification and graphene wrapping. After the graphene wrapping process, the FT-IR spectrum of the $Si_{60}Sn_{12}Ce_{18}Fe_5Al_3Ti_2$ NFs@rGO showed an increase in two characteristic absorption peaks at 1130 and 1100 cm^{-1}, which are associated with the C—N stretching vibration and the C—O stretching vibration stemming from the secondary amine and secondary alcohol in the rGO, respectively. This result also indicates that the APS components which form the amide bond with GO are well grafted onto the surfaces of the $Si_{60}Sn_{12}Ce_{18}Fe_5Al_3Ti_2$ NFs. Moreover, the eliminated peak, which is related to an epoxy ring, was confirmed at ~1250 cm^{-1}, most likely resulted from the epoxy ring-opening reaction.[44,51] Therefore, these structural differences between each step represent crucial evidence of the graphene wrapping of the $Si_{60}Sn_{12}Ce_{18}Fe_5Al_3Ti_2$ NFs.

Electrochemical Characterization of $Si_{60}Sn_{12}Ce_{18}Fe_5Al_3Ti_2$ NFs and $Si_{60}Sn_{12}Ce_{18}Fe_5Al_3Ti_2$ NFs@rGO. Figure 5a shows the charge/discharge cycling performance of the $Si_{60}Sn_{12}Ce_{18}Fe_5Al_3Ti_2$ NFs before and after the graphene modification process. The $Si_{60}Sn_{12}Ce_{18}Fe_5Al_3Ti_2$ NFs exhibited an irreversible capacity of 353.17 mAh g^{-1} at 0.5C and corresponding low initial Coulombic efficiency of 56.99%. For the $Si_{60}Sn_{12}Ce_{18}Fe_5Al_3Ti_2$ NFs@rGO, the irreversible capacity loss is 154.97 mAh g^{-1} (from 719.39 mAh g^{-1} to 564.42 mAh g^{-1}; high Coulombic efficiency, 78.5%) (Figure S7). This difference would be mainly caused by the restricted SEI formation on the graphene layers, which prevents direct contact between the $Si_{60}Al_3Fe_5Ti_2Sn_{12}Ce_{18}$ NFs and the electrolyte. Moreover, the graphene-wrapped NFs show impressive charge/discharge cycling performance levels. The capacity retention of the $Si_{60}Sn_{12}Ce_{18}Fe_5Al_3Ti_2$ NFs is 99.87% from the fifth cycle (409.47 mAh g^{-1}) to the 2000th cycle (408.97 mAh g^{-1}). The $Si_{60}Sn_{12}Ce_{18}Fe_5Al_3Ti_2$ NFs@rGO electrode also exhibits remarkable cycle performance up to 2000 cycles: 570.13 mAh g^{-1} at the fifth cycle and 569.77 mAh g^{-1} at the 2000th cycle (99.93% capacity retention). It was also clearly determined that the cycling capacities of the $Si_{60}Sn_{12}Ce_{18}Fe_5Al_3Ti_2$ NFs@rGO are approximately 200 mAh g^{-1} higher than those of the $Si_{60}Al_3Fe_5Ti_2Sn_{12}Ce_{18}$ NFs throughout the cycling range. This suggests that a greater electrochemically active area could be accessed with the help of the graphene.

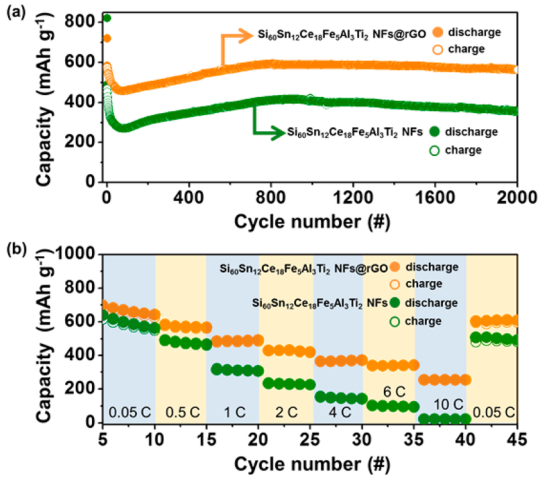

Figure 5. (a) Comparative charge/discharge cycling data of the $Si_{60}Sn_{12}Ce_{18}Fe_5Al_3Ti_2$ NFs and $Si_{60}Sn_{12}Ce_{18}Fe_5Al_3Ti_2$ NFs@rGO at a current density of 0.5C. (b) Rate capability tests at rates varying from 0.05C to 10C (the charge current density was fixed at 0.05C from the fifth cycle to the 40th cycle). The cells were cycled at 0.05C for the initial five cycles in order to activate the cells and stabilize the electrochemical electrode/electrolyte interface. Here, the capacities were calculated on the basis of the total weight of the electrode. All coin cells were cycled between 0.01 and 2.5 V *vs* Li^+/Li.

In addition, graphene wrapping can be extremely beneficial to a high electrical conductivity of the overall electrode, which enables high power rate capability levels (Figure 5b). The $Si_{60}Sn_{12}Ce_{18}Fe_5Al_3Ti_2$ NFs show notable capacity drops upon stepwise rate increases from 1C to 10C. This inferior rate stability may have originated from surface oxidation and from the thick SEI layers of the NFs, which increase the interfiber contact resistance. The $Si_{60}Sn_{12}Ce_{18}Fe_5Al_3Ti_2$ NFs@rGO, on the other hand, show specific discharge capacities of 432, 370, 340, and 255 mAh g^{-1} at 2, 4, 6, and 10C rates (1C = 1.0 A g^{-1}), respectively, which are extremely fast rates for metallic anode materials. Remarkably, there was no decay in the cycling capacities, with Coulombic efficiencies of ~100% at an extremely high current density of 4000 mA g^{-1}, allowing these devices to compete with the most successful commercial graphite anodes. Moreover, the capacity at 0.05C is fully recovered after 35 cycles of the rate capability test, indicating that the electrical and structural integrity levels of the $Si_{60}Sn_{12}Ce_{18}Fe_5Al_3Ti_2$ NFs@rGO are preserved during the high-rate Li^+ insertion/extraction cycles. It is believed that the excellent long-term cycle life and rate capability of $Si_{60}Sn_{12}Ce_{18}Fe_5Al_3Ti_2$ NFs@rGO can be interpreted as synergistic effects of (i) the low-strain Si-based metallic glass NFs, and (ii) highly conductive graphene layers coated onto the 3-D NF network with incredibly stable SEI layers. We suggest that this novel balanced structure design is the main origin of the enhanced electrochemical performance.

***Ex Situ* Investigation into Behavior of SEI Layer during Electrochemical Cycling.** To probe the interfacial,

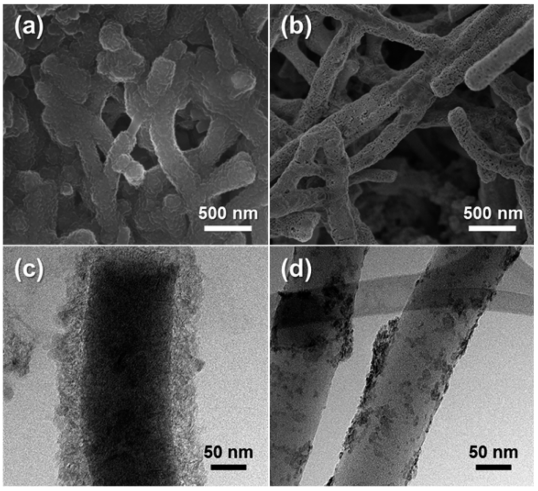

Figure 6. *Ex situ* (a) SEM and (c) TEM images of the first fully lithiated $Si_{60}Sn_{12}Ce_{18}Fe_5Al_3Ti_2$ NFs. *Ex situ* (b) SEM and (d) TEM images of the first fully lithiated state of the $Si_{60}Sn_{12}Ce_{18}Fe_5Al_3Ti_2$ NFs@rGO.

morphological, and structural changes during cycling, SEM and TEM images of the fibers in the electrodes were taken after the first lithiation step, as shown in Figure 6. It is also noteworthy that the electrode of the $Si_{60}Sn_{12}Ce_{18}Fe_5Al_3Ti_2$ NFs is covered with thick SEI layers, as shown in Figure 6a, with a thickness of approximately 50 nm (Figure 6c). However, the $Si_{60}Sn_{12}Ce_{18}Fe_5Al_3Ti_2$ NFs@rGO shows negligible SEI layers, and its morphology is also dense and localized, as indicated in Figure 6b and 6d. These results suggest that there is a great difference between the two samples in terms of the degree of surface reactivity. In the $Si_{60}Sn_{12}Ce_{18}Fe_5Al_3Ti_2$ NFs@rGO, the surface is protected by the basal plane of the graphene layers. The basal plane can be conceived as a chemically inert layer, as it requires much energy to induce surface defects.[52] Moreover, a nondefective surface basal plane should not store lithium ions, thus also reducing the chemical and electrochemical reactions at the electrochemical interface. Lastly, the graphene layer can minimize the electrochemical surface area change during lithiation while, in the bare sample, the bare active material surface should be exposed every time the microstructure changes due to lithium insertion. This is analogous to clothes, which protect the skin from direct exposure to the environment and provide room to accommodate physical body motions inside (a detailed discussion is given in Figure S8). Here, we suggest that the graphene layer could be a multifunctional component that can increase the electrical conductivity of the active material as well as stabilize the electrochemical interface structure.

Electrochemical impedance spectroscopy (EIS) tests of the $Si_{60}Sn_{12}Ce_{18}Fe_5Al_3Ti_2$ NFs and $Si_{60}Sn_{12}Ce_{18}Fe_5Al_3Ti_2$ NFs@rGO electrodes after 100th cycles were performed, as shown in Figure 7. The equivalent circuit

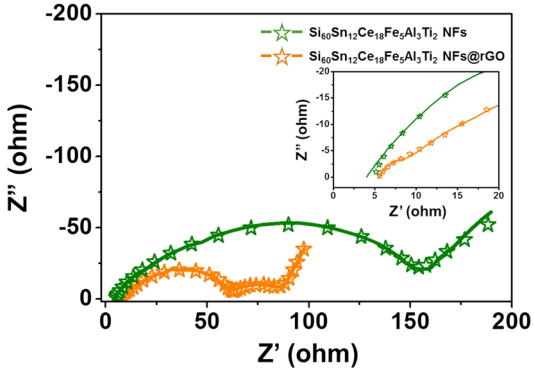

Figure 7. Nyquist plots of the $Si_{60}Sn_{12}Ce_{18}Fe_5Al_3Ti_2$ NFs (green) and $Si_{60}Sn_{12}Ce_{18}Fe_5Al_3Ti_2$ NFs@rGO (orange) after the 100th discharge, presented with fitted curves. The data was evaluated by a different equivalent circuits.

TABLE 1. Fitted Electrochemical Impedance Component Values of the $Si_{60}Sn_{12}Ce_{18}Fe_5Al_3Ti_2$ NFs and $Si_{60}Sn_{12}Ce_{18}Fe_5Al_3Ti_2$ NFs@rGO as Calculated from the Different Equivalent Circuit Models Presented in Figure S9

		R_{SEI} (Ω)	R_{CT-1} (Ω)	R_{CT-2} (Ω)	R_P (Ω)
$Si_{60}Sn_{12}Ce_{18}Fe_5Al_3Ti_2$	100th cycle	43.19	112.27	—	2.831×10^{10}
$Si_{60}Sn_{12}Ce_{18}Fe_5Al_3Ti_2$@rGO	100th cycle	3.11	54.03	22.37	1.644×10^{9}

models appeared three or four parallel RC (resistance-capacitor) circuits in series (Figure S9). R_E represents the ohmic resistance of the cell; R_{SEI} is the overall inner resistance of the SEI layer; and R_{CT} and R_P represent the charge transfer resistance and phase transformation resistance, respectively. The constant phase elements (CPE_{SEI}, CPE_{DL} and CPE_P) represent the capacitances of the SEI layer, the double layer, and phase transformation as parallel capacitances, respectively. The calculated parameter values are listed in Table 1. The first two semicircles respectively indicate the R_{SEI} and R_{CT-1} and show that the $Si_{60}Sn_{12}Ce_{18}Fe_5Al_3Ti_2$ NFs@rGO clearly has lower overall impedance values. Considering the R_{SEI} value calculated from the equivalent circuit, the SEI resistance of the $Si_{60}Sn_{12}Ce_{18}Fe_5Al_3Ti_2$ NFs@rGO (3.11 Ω) was dramatically reduced compared to the $Si_{60}Sn_{12}Ce_{18}Fe_5Al_3Ti_2$ NFs@rGO (43.19 Ω) after 100 cycles. These results successfully support the contrast shown in the TEM images in Figure 6c and 6d. Besides the low R_{SEI}, the R_{CT-1} could decrease from 112.27 Ω to 54.03 Ω by employing highly conductive rGO layer. The third semicircle (R_{CT-2}) of the $Si_{60}Sn_{12}Ce_{18}Fe_5Al_3Ti_2$ NFs@rGO is stemmed from the APS-functional layer which serves as electrochemical resistance, thus it may impede Li^+ transfer through the layer. This is the reason why the equivalent circuit models between the two samples are different as shown in Figure S9. Nonetheless, the layer does not significantly impede the ionic transfer, as suggested by the low impedance values.

CONCLUSION

In conclusion, we designed graphene-wrapped silicon-based metallic glass alloy nanofibers to overcome the inherent structural problems of silicon anodes for lithium-ion batteries. The compositionally optimized nanofibers bring an amorphous phase with a homogeneous atomic distribution, which is ideal for stable electrochemical cycling. $Si_{60}Sn_{12}Ce_{18}Fe_5Al_3Ti_2$ NFs have a high Li storage capacity and a good cycle lifetime (~1000 mAh g^{-1} at 50 mA g^{-1} after 400 cycles) of nearly one year. With their highly robust properties based on a metallic glass phase, the graphene shell can play a critical role in minimizing and stabilizing the SEI layers, thus promoting electrical transport. It demonstrated an ultralong cycle lifetime (569.77 mAh g^{-1}, 99.93% capacity retention after 2000 cycles at 500 mA g^{-1}). Our novel concept of the design of a Si anode is promising, especially because, for the first time, it combines the structural advantages of Si-based metallic glass nanofibers and the interfacial stability levels of a graphene surface-protection layer. We expect that the attractive metallic glass nanofiber will shed light on new applications for nanostructured metallic glass materials.

METHODS

Materials. 1.493 g of 3-aminopropyltriethoxysilane ($C_9H_{23}NO_3Si$, 98%, Alfa Aesar., Ltd., USA), 0.478 g of Tin(IV) acetate ($Sn(CH_3CO_2)_4$, Sigma-Aldrich Co., Ltd., USA), 0.081 g of aluminum chloride hexahydrate ($AlCl_3 \cdot 6H_2O$ 99%, Sigma-Aldrich Co., Ltd., USA), 0.076 g of titanium(IV) butoxide ($Ti[O(CH_2)_3CH_3]_4$, 99%, Sigma-Aldrich Co., Ltd., USA), 0.227 g of iron(III) nitrate nonahydrate ($Fe(NO_3)_3 \cdot 9H_2O$, 98+%, Sigma-Aldrich Co., Ltd., USA) and 0.642 g of cerium(III) acetate hydrate ($Ce(CH_3CO_2)_3 \cdot xH_2O$, 99.999%, Sigma-Aldrich Co., Ltd., USA) were used as precursors of the Si-based multicomponent amorphous alloy nanofibers. 1.2 g of polyvinylpyrrolidone (PVP, M_w = 1 300 000, Sigma-Aldrich Co., Ltd., USA) was used as the spinning media. 3.5 g of *N*,*N*-dimethylformamide (DMF, 99.8%, Sigma-Aldrich Co., Ltd., USA) and 7.5 g of distilled water were used as a mixed solvent for dissolving the precursors, and 0.5 g of acetic acid was used as a catalyst. The graphene oxide solution in this study (GO, 2 mg/mL dispersion in H_2O, Sigma-Aldrich Co., Ltd., USA) was used without any treatment.

Synthesis of the $Si_{60}Al_3Fe_5Ti_2Sn_{12}Ce_{18}$ NFs. The precursors and PVP were dissolved in DMF and distilled water. The solution was stirred at room temperature for 8 h. The blended solution was electrospun with conventional electrospinning equipment (NanoNC, ESR200RD). The flow rate of the solution was 10 μL/min. The needle used had a gauge number of 27. The needle-to-drum collector distance was 18 cm and a high voltage of 20 kV was applied between the needle and the drum collector during the electrospinning process. The collected electrospun $Si_{60}Al_3Fe_5Ti_2Sn_{12}Ce_{18}$ NFs were thermally heated to 700 °C for 2 h under a reducing gas atmosphere (5% H_2 and 95% N_2).

Functionalization and Graphene Wrapping of the $Si_{60}Sn_{12}Ce_{18}Fe_5Al_3Ti_2$ NFs@rGO. The $Si_{60}Sn_{12}Ce_{18}Fe_5Al_3Ti_2$ NFs were homogeneously dispersed in 25 mL of toluene after sonication for 30 min. Additional toluene and 1.5 mL of APS were added to the solution, after which it was refluxed in an N_2 atmosphere for 24 h at 110 °C to functionalize the surfaces of the $Si_{60}Sn_{12}Ce_{18}Fe_5Al_3Ti_2$ NFs. When an amount of 56 mg of the functionalized $Si_{60}Sn_{12}Ce_{18}Fe_5Al_3Ti_2$ NFs was mixed together with the GO solution (0.16 mg/mL), GO-wrapped $Si_{60}Sn_{12}Ce_{18}Fe_5Al_3Ti_2$ NFs were synthesized *via* the electrostatic interaction between the GO and the $Si_{60}Sn_{12}Ce_{18}Fe_5Al_3Ti_2$ NFs in the aqueous solution under mild stirring. After 30 min, 0.6 mL of hydrazine monohydrate was added to the solution and it was mildly stirred for 5 h to reduce the GO on the surface of $Si_{60}Sn_{12}Ce_{18}Fe_5Al_3Ti_2$ NFs chemically. $Si_{60}Sn_{12}Ce_{18}Fe_5Al_3Ti_2$ NFs@rGO was obtained after subsequent washing and drying steps.

Material Characterizations. The morphologies of the $Si_{60}Sn_{12}Ce_{18}Fe_5Al_3Ti_2$ NFs and the $Si_{60}Sn_{12}Ce_{18}Fe_5Al_3Ti_2$ NFs@rGO were investigated by field-emission scanning electron microscopy (FE-SEM, Nova 230 and Magellan 400, FEI) and with a transmission electron microscope (TEM, Tecnai F30 S-Twin, FEI). The investigation of the amorphous phase was carried out by X-ray diffraction (XRD, D/MAX-RC, Rigaku) with Cu Kα (λ = 1.54 Å) radiation and a high-resolution TEM (HR-TEM) analysis. The elemental analysis of the $Si_{60}Sn_{12}Ce_{18}Fe_5Al_3Ti_2$ NFs@rGO was conducted by means of energy-dispersive X-ray spectroscopy (EDS). Raman spectroscopy was carried out to investigate the graphene sheets using a LabRAM HR UV/vis/NIR PL by Horiba Jobin Yvon of France. To confirm the functional groups and the rGO attachment characteristics, Fourier transform infrared spectroscopy (FT-IR) was carried out using an IFS66 V/S & Hyperion 3000 device by Bruker Optics of Germany. The general oxide species and a quantitative analysis of the oxygen used here were verified by X-ray photoelectron spectroscopy (XPS, Thermo VG Scientific, MultiLab 2000) and by an elemental analysis (EA, Thermo Scientific, Flash 2000 series). The accuracy of the multiple components with a complex atomic ratio was measured by an inductively coupled plasma analyzer (ICP-OES, Thermo Scientific iCAP 6300).

Cell Assembly and Electrochemical Characterization. The electrode of the $Si_{60}Sn_{12}Ce_{18}Fe_5Al_3Ti_2$ NFs was prepared by casting a slurry consisting of 75 wt % of active materials, 15 wt % of carbon black (super P, Alfa Aesar) and 10 wt % of polyvinylidene fluoride (PVDF, Aldrich) as a binder onto a copper foil. The mass loading of the Si-based metallic glass NFs were 1 ± 0.1 mg cm^{-2}. After drying the electrode in a vacuum oven at 80 °C, CR2032 coin-type cells were assembled in an Ar-filled glovebox with the electrodes. Lithium metal was used as the counter electrode, and Celgard 2400 was used as the separator. One M of $LiPF_6$ at a 1:1 volume mixture of ethylene carbonate to diethylene carbonate (Soulbrain Co., Ltd., Korea) was used as the electrolyte. The electrochemical performance levels were tested by carrying out galvanostatic charge−discharge experiments at different current densities between cutoff potentials of 2.5 and 0.01 V *vs* Li/Li^+ with a battery testing system (Multi-Cycling Battery Test System, USA).

Conflict of Interest: The authors declare no competing financial interest.

Acknowledgment. This work was supported by Korea CCS R&D Center (KCRC) grant funded by the Korea government (Ministry of Science, ICT & Future Planning) (No. NRF-2014M1A8A1049303).

Supporting Information Available: Additional SEM and TEM images of the $Si_{60}Sn_{12}Ce_{18}Fe_5Al_3Ti_2$ NFs@rGO, additional XRD data, the XPS analysis data pertaining to the $Si_{60}Sn_{12}Ce_{18}Fe_5Al_3Ti_2$ NFs, a STEM image including the line profile of the $Si_{60}Sn_{12}Ce_{18}Fe_5Al_3Ti_2$ NFs, the *ex situ* SEM image analysis data, and additional electrochemical data. The Supporting Information is available free of charge on the ACS Publications website at DOI: 10.1021/acsnano.5b01402.

REFERENCES AND NOTES

1. McDowell, M. T.; Lee, S. W.; Nix, W. D.; Cui, Y. 25th Anniversary Article: Understanding the Lithiation of Silicon and Other Alloying Anodes for Lithium-Ion Batteries. *Adv. Mater.* **2013**, *25*, 4966–4985.

2. Obrovac, M. N.; Krause, L. J. Reversible Cycling of Crystalline Silicon Powder. *J. Electrochem. Soc.* **2007**, *154*, A103–A108.
3. Liu, X. H.; Zheng, H.; Zhong, L.; Huang, S.; Karki, K.; Zhang, L. Q.; Liu, Y.; Kushima, A.; Liang, W. T.; Wang, J. W.; *et al.* Anisotropic Swelling and Fracture of Silicon Nanowires during Lithiation. *Nano Lett.* **2011**, *11*, 3312–3318.
4. Beaulieu, L. Y.; Eberman, K. W.; Turner, R. L.; Krause, L. J.; Dahn, J. R. Colossal Reversible Volume Changes in Lithium Alloys. *Electrochem. Solid-State Lett.* **2001**, *4*, A137–A140.
5. Lee, Y. M.; Lee, J. Y.; Shim, H. T.; Lee, J. K.; Park, J. K. SEI Layer Formation on Amorphous Si Thin Electrode during Precycling. *J. Electrochem. Soc.* **2007**, *154*, A515–A519.
6. Cho, J. H.; Picraux, S. T. Silicon Nanowire Degradation and Stabilization during Lithium Cycling by SEI Layer Formation. *Nano Lett.* **2014**, *14*, 3088–3095.
7. Aricò, A. S.; Bruce, P.; Scrosati, B.; Tarascon, J.; Schalkwijk, W. V. A. N. Nanostructured Materials for Advanced Energy Conversion and Storage Devices. *Nat. Mater.* **2005**, *4*, 366–377.
8. Oumellal, Y.; Delpuech, N.; Mazouzi, D.; Dupré, N.; Gaubicher, J.; Moreau, P.; Soudan, P.; Lestriez, B.; Guyomard, D. The Failure Mechanism of Nano-Sized Si-Based Negative Electrodes for Lithium-Ion Batteries. *J. Mater. Chem.* **2011**, *21*, 6201–6208.
9. Liu, X. H.; Wang, J. W.; Huang, S.; Fan, F.; Huang, X.; Liu, Y.; Krylyuk, S.; Yoo, J.; Dayeh, S. A.; Davydov, A. V.; *et al. In Situ* Atomic-Scale Imaging of Electrochemical Lithiation in Silicon. *Nat. Nanotechnol.* **2012**, *7*, 749–756.
10. Wang, C. M.; Li, X.; Wang, Z.; Xu, W.; Liu, J.; Gao, F.; Kovarik, L.; Zhang, J. G.; Howe, J.; Burton, D. J.; *et al. In Situ* TEM Investigation of Congruent Phase Transition and Structural Evolution of Nanostructured Silicon/Carbon Anode for Lithium-Ion Batteries. *Nano Lett.* **2012**, *12*, 1624–1632.
11. McDowell, M. T.; Lee, S. W.; Harris, J. T.; Korgel, B. a; Wang, C.; Nix, W. D.; Cui, Y. *In Situ* TEM of Two-Phase Lithiation of Amorphous Silicon Nanospheres. *Nano Lett.* **2013**, *13*, 758–764.
12. Tritsaris, G. A.; Zhao, K.; Okeke, O. U.; Kaxiras, E. Diffusion of Lithium in Bulk Amorphous Silicon: A Theoretical Study. *J. Phys. Chem. C* **2012**, *116*, 22212–22216.
13. Ye, J. C.; Lu, J.; Liu, C. T.; Wang, Q.; Yang, Y. Atomistic Free-Volume Zones and Inelastic Deformation of Metallic Glasses. *Nat. Mater.* **2010**, *9*, 619–623.
14. Yavari, A. R.; Moulec, A. L.; Inoue, A.; Nishiyama, N.; Lupu, N.; Matsubara, E.; Botta, W. J.; Vaughan, G.; Michiel, M. D.; Kvick, Å. Excess Free Volume in Metallic Glasses Measured by X-Ray Diffraction. *Acta Mater.* **2005**, *53*, 1611–1619.
15. Ko, M.; Chae, S.; Jeong, S.; Oh, P.; Cho, J. Elastic a-Silicon Nanoparticle Backboned Graphene Hybrid as a Self-Compacting Anode for High-Rate Lithium-Ion Batteries. *ACS Nano* **2014**, *8*, 8591–8599.
16. Cui, L.; Ruffo, R.; Chan, C. K.; Peng, H.; Cui, Y. Crystalline-Amorphous Core-Shell Silicon Nanowires for High Capacity and High Current Battery Electrodes. *Nano Lett.* **2009**, *9*, 491–495.
17. Obrovac, M. N.; Christensen, L.; Le, D. B.; Dahn, J. R. Alloy Design for Lithium-Ion Battery Anodes. *J. Electrochem. Soc.* **2007**, *154*, A849–A855.
18. Fleischauer, M. D.; Topple, J. M.; Dahn, J. R. Combinatorial Investigations of Si-M (M = Cr + Ni, Fe, Mn) Thin Film Negative Electrode Materials. *Electrochem. Solid-State Lett.* **2005**, *8*, A137–A140.
19. Beaulieu, L. Y.; Hewitt, K. C.; Turner, R. L.; Bonakdarpour, A.; Abdo, A. A.; Christensen, L.; Eberman, K. W.; Krause, L. J.; Dahn, J. R. The Electrochemical Reaction of Li with Amorphous Si-Sn Alloys. *J. Electrochem. Soc.* **2003**, *150*, A149–A156.
20. Hatchard, T. D.; Dahn, J. R.; Trussler, S.; Fleischauer, M.; Bonakdarpour, A.; Mueller-Neuhaus, J. R.; Hewitt, K. C. The Amorphous Range in Sputtered Si-Al-Sn Films. *Thin Solid Films* **2003**, *443*, 144–150.
21. Hatchard, T. D.; Topple, J. M.; Fleischauer, M. D.; Dahn, J. R. Electrochemical Performance of SiAlSn Films Prepared by Combinatorial Sputtering. *Electrochem. Solid-State Lett.* **2003**, *6*, A129–A132.
22. Fleischauer, M. D.; Obrovac, M. N.; Dahn, J. R. Simple Model for the Capacity of Amorphous Silicon-Aluminum-Transition Metal Negative Electrode Materials. *J. Electrochem. Soc.* **2006**, *153*, A1201–A1205.
23. Dahn, J. R.; Mar, R. E.; Fleischauer, M. D.; Obrovac, M. N. The Impact of the Addition of Rare Earth Elements to $Si_{1-x}Sn_x$ Negative Electrode Materials for Li-Ion Batteries. *J. Electrochem. Soc.* **2006**, *153*, A1211–A1220.
24. Li, J.; Dahn, H. M.; Sanderson, R. J.; Todd, A. D. W.; Dahn, J. R. Impact of Rare Earth Additions on Transition Metal Oxides as Negative Electrodes for Lithium-Ion Batteries. *J. Electrochem. Soc.* **2008**, *155*, A975–A981.
25. Obrovac, M. N.; Chevrier, V. L. Alloy Negative Electrodes for Li-Ion batteries. *Chem. Rev.* **2014**, *114*, 11444–11502.
26. Xiao, X.; Wang, J. S.; Liu, P.; Sachdev, A. K.; Verbrugge, M. W.; Haddad, D.; Balogh, M. P. Phase-Separated Silicon−Tin Nanocomposites for High Capacity Negative Electrodes in Lithium-Ion Batteries. *J. Power Sources* **2012**, *214*, 258–265.
27. Shin, J.; Ryu, W. H.; Park, K.; Kim, I. D. Morphological Evolution of Carbon Nanofibers Encapsulating SnCo Alloys and Its Effect on Growth of the Solid Electrolyte Interphase Layer. *ACS Nano* **2013**, *7*, 7330–7341.
28. Obrovac, M.; Christensen, L. Alloy Composition for Lithium-Ion Batteries, US Patent 7,851,085 (Application Number: 2007/0020521), Dec. 14, 2010 (Application Date: Jan. 25, 2007).
29. Tian, L.; Cheng, Y. Q.; Shan, Z. W.; Li, J.; Wang, C. C.; Han, X. D.; Sun, J.; Ma, E. Approaching the Ideal Elastic Limit of Metallic Glasses. *Nat. Commun.* **2012**, *3*, 609.
30. Song, T.; Hu, L.; Paik, U. One-Dimensional Silicon Nanostructures for Li Ion Batteries. *J. Phys. Chem. Lett.* **2014**, *5*, 720–731.
31. Su, X.; Wu, Q.; Li, J.; Xiao, X.; Lott, A.; Lu, W.; Sheldon, B. W.; Wu, J. Silicon-Based Nanomaterials for Lithium-Ion Batteries: A Review. *Adv. Energy Mater.* **2013**, *4*, 1–23.
32. Wu, H.; Cui, Y. Designing Nanostructured Si Anodes for High Energy Lithium-Ion Batteries. *Nano Today* **2012**, *7*, 414–429.
33. Mukherjee, S.; Sekol, R. C.; Carmo, M.; Altman, E. I.; Taylor, A. D.; Schroers, J. Tunable Hierarchical Metallic-Glass Nanostructures. *Adv. Funct. Mater.* **2013**, *23*, 2708–2713.
34. Chan, C. K.; Peng, H.; Liu, G.; McIlwrath, K.; Zhang, X. F.; Huggins, R. A.; Cui, Y. High-Performance Lithium Battery Anodes Using Silicon Nanowires. *Nat. Nanotechnol.* **2008**, *3*, 31–35.
35. Yoo, H.; Lee, J.; Kim, H.; Lee, J.; Cho, J.; Park, S. Helical Silicon/Silicon Oxide Core-Shell Anodes Grown onto the Surface of Bulk Silicon. *Nano Lett.* **2011**, *11*, 4324–4328.
36. Ge, M.; Rong, J.; Fang, X.; Zhou, C. Porous Doped Silicon Nanowires for Lithium-Ion Battery Anode with Long Cycle Life. *Nano Lett.* **2012**, *12*, 2318–2323.
37. Cui, L.; Yang, Y.; Hsu, C.; Cui, Y. Carbon-Silicon Core-Shell Nanowires as High Capacity Electrode for Lithium-Ion Batteries. *Nano Lett.* **2009**, *9*, 3370–3374.
38. Kim, G.; Jeong, S.; Shin, J.; Cho, J.; Lee, H. 3D Amorphous Silicon on Nanopillar Copper Electrodes as Anodes for High- Rate Lithium-Ion Batteries. *ACS Nano* **2014**, *8*, 1907–1912.
39. Kim, C.; Ko, M.; Yoo, S.; Chae, S.; Choi, S.; Lee, E.-H.; Ko, S.; Lee, S.-Y.; Cho, J.; Park, S. Novel Design of Ultra-Fast Si Anodes for Li-Ion Batteries: Crystalline Si@Amorphous Si Encapsulating Hard Carbon. *Nanoscale* **2014**, *6*, 10604–10610.
40. Cavaliere, S.; Subianto, S.; Savych, I.; Jones, D. J.; Rozière, J. Electrospinning: Designed Architectures for Energy Conversion and Storage Devices. *Energy Environ. Sci.* **2011**, *4*, 4761–4785.
41. Yoo, J. K.; Kim, J.; Jung, Y. S.; Kang, K. Scalable Fabrication of Silicon Nanotubes and Their Application to Energy Storage. *Adv. Mater.* **2012**, *24*, 5452–5456.
42. Hwang, T. H.; Lee, Y. M.; Kong, B. S.; Seo, J. S.; Choi, J. W. Electrospun Core-Shell Fibers for Robust Silicon Nanoparticle-Based Lithium-Ion Battery Anodes. *Nano Lett.* **2012**, *12*, 802–807.

43. Wu, H.; Chan, G.; Choi, J. W.; Ryu, I.; Yao, Y.; McDowell, M. T.; Lee, S. W.; Jackson, A.; Yang, Y.; Hu, L.; *et al.* Stable Cycling of Double-Walled Silicon Nanotube Battery Anodes through Solid-Electrolyte Interphase Control. *Nat. Nanotechnol* **2012**, *7*, 310–315.
44. Shin, J.; Park, K.; Ryu, W. H.; Jung, J. W.; Kim, I. D. Graphene Wrapping as a Protective Clamping Layer Anchored to Carbon Nanofibers Encapsulating Si Nanoparticles for a Li-Ion Battery Anode. *Nanoscale* **2014**, *6*, 12718–12726.
45. Wang, B.; Luo, B.; Li, X.; Zhi, L. The Dimensionality of Sn Anodes in Li-Ion Batteries. *Mater. Today* **2012**, *15*, 544–552.
46. Kim, D.; Lee, D.; Kim, J.; Moon, J. Electrospun Ni-Added SnO_2−Carbon Nanofiber Composite Anode for High-Performance Lithium-Ion Batteries. *ACS Appl. Mater. Interfaces* **2012**, *4*, 5408–5415.
47. Schroder, K. W.; Dylla, A. G.; Harris, S. J.; Webb, L. J.; Stevenson, K. J. Role of Surface Oxides in the Formation of Solid-Electrolyte Interphase at Silicon Electrodes for Lithium-Ion Battereis. *ACS Appl. Mater. Interfaces* **2014**, *6*, 21510–21524.
48. Beaulieu, L. Y.; Hatchard, T. D.; Bonakdarpour, A.; Fleischauer, M. D.; Dahn, J. R. Reaction of Li with Alloy Thin Films Studied by *In Situ* AFM. *J. Electrochem. Soc.* **2003**, *150*, A1457–A1464.
49. Kim, S.; Choi, J. H.; Lim, D. S.; Lee, J. H.; Kim, I. D. Phase and Microstructural Evolution of Sn Particles Embedded in Amorphous Carbon Nanofibers and Their Anode Properties in Li-Ion Batteries. *J. Electroceram.* **2014**, *32*, 261–268.
50. Han, X.; Liu, Y.; Jia, Z.; Chen, Y. C.; Wan, J.; Weadock, N.; Gaskell, K. J.; Li, T.; Hu, L. Atomic-Layer-Deposition Oxide Nanoglue for Sodium Ion Batteries. *Nano Lett.* **2014**, *14*, 139–147.
51. Zhou, W.; Zhu, J.; Cheng, C.; Liu, J.; Yang, H.; Cong, C.; Guan, C.; Jia, X.; Fan, H. J.; Yan, Q.; *et al.* A General Strategy toward Graphene@Metal Oxide Core−Shell Nanostructures for High-Performance Lithium Storage. *Energy Environ. Sci.* **2011**, *4*, 4954–4961.
52. Zhou, S.; Bongiorno, A. Origin of the Chemical and Kinetic Stability of Graphene Oxide. *Sci. Rep.* **2013**, *3*, 2484.